Effects of Metal−Ion Complexation for the Self-Assembled Nanocomposite Films Composed of Gold Nanoparticles and 3,8-Bis(terthiophenyl)phenanthroline-Based Dithiols Bridging 1 *μ*m Gap Gold Electrodes: Morphology, Temperature Dependent Electronic Conduction, and Photoresponse

Wei Huang,*,†,‡ Hirofumi Tanaka,‡,§ and Takuji Ogawa*,‡,§

State Key Laboratory of Coordination Chemistry, Coordination Chemistry Institute, Nanjing University−Jinchuan Group Ltd. Joint Laboratory of Metal Chemistry, School of Chemistry and Chemical Engineering, Nanjing University, Nanjing 210093, China, Research Center for Molecular-Scale Nanoscience, Institute for Molecular Science, 5-1 Higashiyama, Myodaiji, Okazaki 444-8787, Japan, and Core Research for Evolutional Science and Technology (CREST) of Japan Science and Technology Agency (JST), Hon-machi 4-1-8, Kawaguchi, Saitama, 332-0012, Japan

Received: December 11, 2007; Revised Manuscript Received: March 21, 2008

3,8-Bis(3′,4′-dibutyl-5″-mercapto-2,2′:5′,2″-terthiophen-5-yl)-1,10-phenanthroline (**2**) with a molecular length of 3.36 nm and its Ru(II), Fe(II), and Cu(II) complexes were treated with *tert*-dodecanethiol-protected active gold nanoparticles (Au-NPs) in an average size of 3.3 nm in the presence of two facing Au electrodes with a 1 × 1 μm^2 gap. Stable self-assembled molecular junctions were produced, wherein dithiols-bridged Au-NPs were chemisorbed to the electrodes by means of Au−S-bonded contacts. SEM and AFM micrographs showed that different morphologies of the films were formed depending on the number of ligand **2** in the molecules and the coordination configurations of transition metal ions. Among them a relatively homogeneous granular thin film was obtained successfully in the case of the $[Ru(bpy)_2]^{2+}$ complex. Temperature-dependent current−voltage measurements for these junctions were performed in the temperature range of 8−300 K. The electronic conduction is dominated by the sum of tunneling and thermal excitation. Classical Arrhenius plots and their linear fits, wherein the temperature-independent tunneling current was deducted, were obtained to determine the average activation energies of these nanodevices. Photoresponsive properties of these self-assembled films were studied at different temperature (80, 160, and 300 K, respectively), where reversible and reproducible photoresponse can be recorded at room temperature in the presence of $[Ru(bpy)_2]^{2+}$ species. The comparison of results before and after metal−ion complexation reveals that the introduction of Ru(II) ion into the metal−molecule system can improve effectively the morphology of the self-assembled films and the overall conductivity, decrease the barrier for activation energy, and enhance the photoresponse of these nanodevices.

1. Introduction

Semiconductors and metal nanoparticles occupy the center of scientific interest because of their unique electronic nature: they follow quantum mechanical rules instead of the laws of classical physics which govern bulk materials.[1] Efforts to understand the physics behind ever-smaller structures have been accompanied in parallel by attempts to exploit such structures for practical applications. The tailored surface chemistries of synthesized nanoparticles with controlled size and composition allow them to be used as model systems for investigating fundamental physics and chemistry of low-dimensional solids and nanoscale materials.[2] Self-assembly is an attractive and facile nanofabrication technique because it provides the means to engineer structures precisely on a nanometer scale over large sample areas. The introduction of synthetic techniques for preparing narrow and tunable size distributions of metal and semiconductor nanoparticles has provided building blocks for assembling ordered 2D monolayers and 3D thin films[3,4] wherein individual molecules work as independent functional units. One of the remarkable features in organic molecules is that each molecule shows characteristic electrical and/or optical properties that are greatly sensitive to its molecular structure and conformation.[5] This allows us to design a wide variety of functional devices. However, direct access to a single molecule and the measurement of its properties are essential for establishing molecular electronics.

There have been a large number of studies[6] on semiconducting molecules which show a wide variety of electrical and optical properties originating from their π-conjugated electrons delocalized over the entire molecular structure. Semiconducting oligothiophenes have attracted growing interest because their conjugated length can be exactly controlled by chemical synthesis of the oligomers. It is noted that thin films of oligothiophenes have been used as active layers in field-effect transistors[7] and light-emitting diodes.[8] On the other hand, derivatives of oligothiophenes are easily obtained since the α-carbon atom of the thiophene ring is active. In our previous report,[9] a series of linear oligothiophene-based terminal dithiols with 3, 6, and 9 thiophene rings in the molecules were first utilized in combination with active Au-NPs bridging 1 μm gap

---

* To whom correspondence should be addressed. E-mail: whuang@nju.edu.cn (W.H.); ogawat@ims.ac.jp (T.O.).

† Nanjing University.

‡ Institute for Molecular Science.

§ Core Research for Evolutional Science and Technology of Japan Science and Technology Agency.

10.1021/jp711635p CCC: $40.75

SCHEME 1: Schematic Diagram of a Self-Assembled Granular Film Consisting of Au-NPs That Were Bridged by Various Dithiols with Different Conformations (Right) Covering the 1 × 1 μm^2 Gap Area between Two Facing Au Electrodes on the SiO_2 Surface

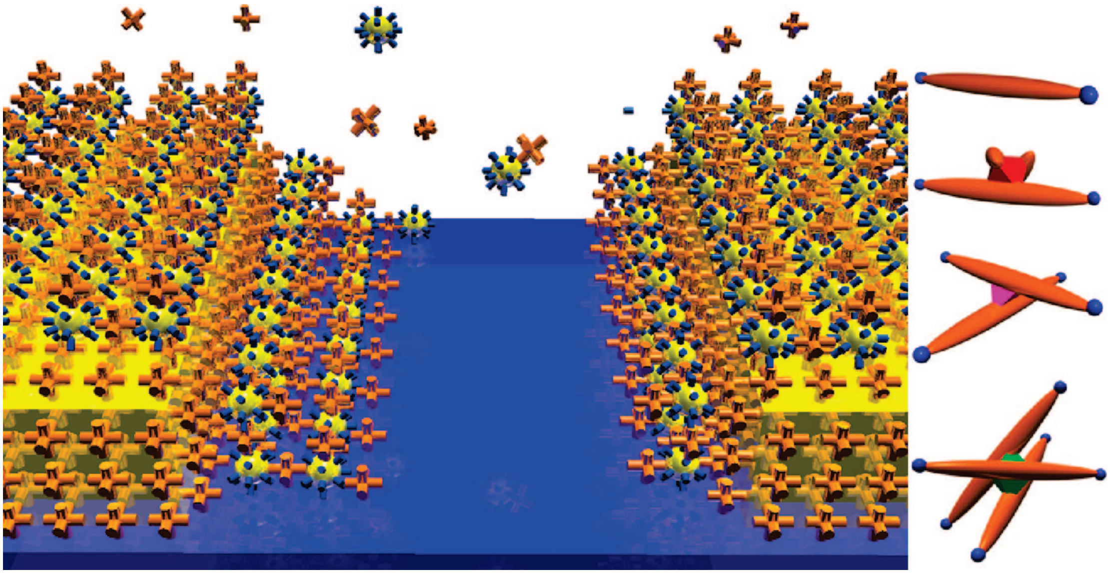

Au electrodes via strong Au−S contacts, and the resulting self-assembled thin films (3−4 layers) exhibited reproducible temperature-dependent *I*−*V* characteristics and photoresponsive properties at low temperature.

The combination of organic conjugated polymers and nanoparticles has also received much attention recently. But the studies of fine-tuning of molecular structures and the comparison of their optoelectric properties, especially by using metal complexation with organic semiconductors that contain metal binding sites within their molecular backbones, are rarely involved. In this work, our motivation is to prepare a 3,8-bis-oligothiophene-substituted 1,10-phenanthroline dithiol molecule, which not only retains the advantages of oligothiophene molecules but also possesses a strong bidentate chelating unit (phenanthroline) in terms of coordination chemistry. Thus, it will be possible for us to introduce a variety of metal ions to control the molecular conformation and the number of thiol groups in each molecule during the process of fabricating self-assembled thin films between Au electrodes with a 1 μm gap (Scheme 1). These complex fragments as part of the nanoparticle ligand system make the electric and optical properties of the resulting semiconductor films very interesting due to different electronic transport conditions before and after metal−ion complexation, which is suggested to be an important issue in molecular electronics. In this paper, we report (a) the single-crystal structure of the precursor ligand, which is the first solid structure of a heterocycle-substituted phenanthroline compound, (b) SEM and AFM characterizations of the self-assembled films fabricated from its dithiol and the corresponding Ru(II), Fe(II), and Cu(II) complexes bearing different molecular configurations and numbers of thiol groups via in situ thiol-to-thiol ligand exchange with *tert*-dodecanethiol capped active Au-NPs in the presence of 1 × 1 μm^2 gap Au electrodes, (c) temperatur-e and voltage-dependent conductivity, possible electronic conduction mechanisms, and comparison between these composite films before and after metal−ion complexation, and (d) the effects on the enhancement of the generation of photocurrent by means of metal−ion complexation by comparing the *I*−*V* and *I*−*T* curves with and without irradiation at different temperatures (80, 160, and 300 K).

2. Results and Discussion

2.1. Synthesis and Spectral Characterization. Successful preparation of dithiol **2** (3,8-bis(3′,4′-dibutyl-5″-mercapto-2,2′:5′,2″-terthiophen-5-yl)-1,10-phenanthroline) by the reduction of $LiAlH_4$, which is almost quantitative, can be monitored by the thin layer chromatogram (TLC) method and verified by the presence of a new single peak at 3.74 ppm in the ^{1}H NMR spectrum in comparison with the starting material. The infrared spectrum for ferrous complex **4** shows a characteristic absorption of thiocyanate anion at 2111 cm^{-1}, while the IR spectra of **5** and **6** exhibit a very strong shoulder as well as medium peaks at 1104, 1099, and 622 cm^{-1} (**5**) and 1105, 1087, and 622 cm^{-1} (**6**) corresponding to the typical absorptions of perchlorate anions.[10]

UV−vis spectra of **4**, **5**, and **6** in their dichloromethane solutions were obtained to verify the complexation and to compare the differences among them (Figure 1). In comparison with the spectrum of the Ru(II) complex **3** (a broad and intense metal ligand charge transfer (MLCT) peak at 442 nm), red shifts of 6, 33, and 27 nm were observed for **4** (448 nm), **5** (475 nm),

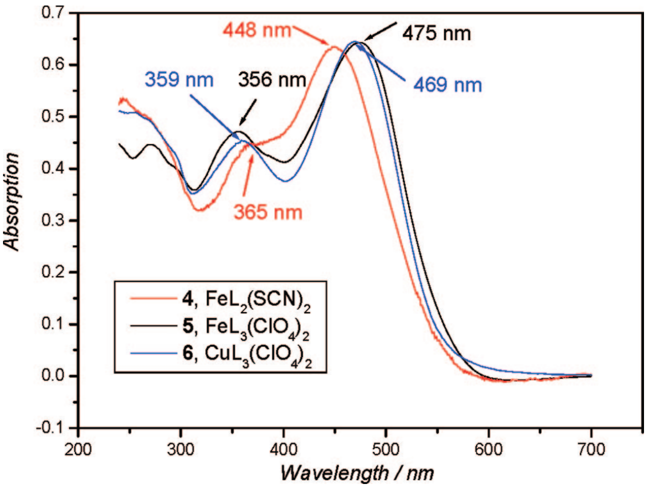

Figure 1. Electronic absorption spectra for **4** (red line), **5** (black line), and **6** (blue line) in dichloromethane solutions.

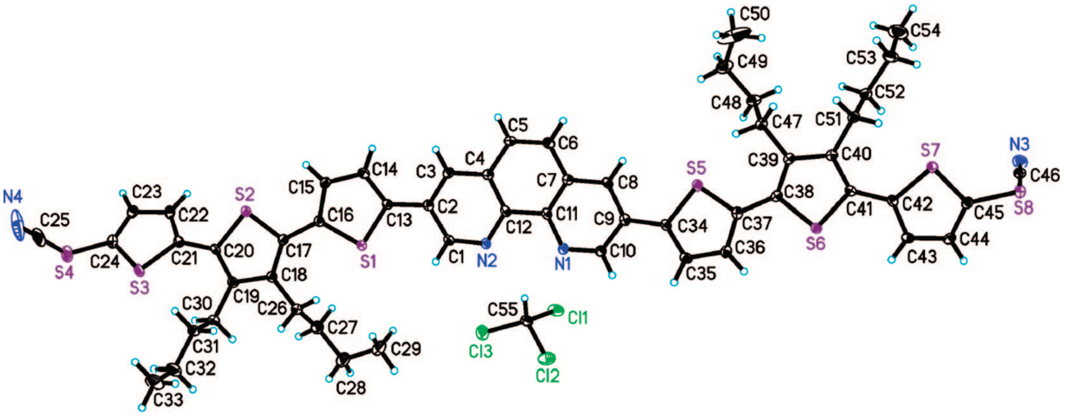

Figure 2. ORTEP diagram (30% thermal probability) of the molecular structure of **1**·$\mathbf{CHCl_3}$ with the atom-numbering scheme.

and **6** (469 nm), respectively, indicative of the increase in the number of ligand **1** in the complexes. The peaks at 356–365 can be assigned to the delocalized $\pi-\pi^*$ transition of thiophene rings, which are analogous to that of the same oligothiophene unit at 359 nm.[11] Compared to the conventional strength of the MLCT,[12] our complexes demonstrated relatively strong absorptions, which suggest that the energy levels were essentially localized in the ligand backbone and the transition metal centers.

Molecular ion peaks of complexes **3**–**6** were verified by the fast atom bombing mass spectra (FAB-MS) method. The dithiol coordination complexes **7**–**10** were synthesized in situ and used directly in the next self-assembly to avoid contamination; however, they were determined by electrospray ionization mass spectra (ESI-MS) to verify the existence of molecular ion peaks of coordination complexes. To obtain good films, all dithiols, active Au-NPs in a narrow size distribution, and gold electrodes were freshly prepared prior to use. Successful preparation of self-assembled films in black via thiol-to-thiol exchange reaction, which were insoluble in chloroform and which could easily be checked by optical microscopy and SEM, was verified based on the conductance between the Au-electrodes. For the case of **14** and **15** where six thiol groups are present in the molecules, black precipitates were obtained after 0.5 h due to the aggregation of the molecules and Au-NPs when the same concentration of dithiol was used.

2.2. Single-Crystal Structure of 3,8-Bis(3′,4′-dibutyl-5″-thiocyanato-2,2′:5′,2″- terthiophen-5-yl)-1,10-phenanthroline in Its Monochloroform Form (1·$\mathbf{CHCl_3}$). X-ray diffraction studies on **1**·$CHCl_3$ indicate that it crystallizes in the triclinic space group $P\bar{1}$ and the whole molecule presents a straight-line motif. As illustrated in Figure 2, six thiophene rings adopt *all-anti* conformations toward the central phenanthroline ring but they are not coplanar because of the steric crowding effect of *n*-butyl aliphatic chains. These alkyl chains bonded to their respective thiophene rings are fully extended whereas those bonded to two different thiophene rings adopt a *trans* conformation with respect to the molecular plane. One of the carbon atoms of the *n*-butyl group (C49) is found to be disordered over two positions with site occupancy factors of 0.660 and 0.340, respectively. The dihedral angles between the phenanthroline ring and two adjacent thiophene rings are 5.6° and 20.6°, and those between the middle alkyl substituted thiophene rings and their neighboring rings are 15.7° (inner), 23.4° (outer) and 26.7° (inner), 4.7° (outer), respectively. Two essentially linear thiocyanate groups [S4–C25–N4, 178.1(8)° and S8–C46–N3, 179.0(5)°] are nearly perpendicular to their thiophene rings with the bond angles at 91.9(2)° and 99.1(2)°, respectively, and they are positioned at each side of the molecular plane. Two terminal sulfur atoms (S4 and S8) lie almost in the molecular plane with a separation of 3.36 nm that is analogous to the size of the Au-NPs used in this study. In addition, one chloroform molecule is linked to the two nitrogen atoms of phenanthroline by C–H···N type hydrogen bonding interactions, with the related data and translations of symmetry codes to equivalent positions listed as follows: C55–H55···N1, D···A, 2.36 Å, H···A, 3.180(6) Å, 140.0°; C55–H55···N2, D···A, 2.41 Å, H···A, 3.251(7) Å, 144.0°.

It is worth noting that $\pi-\pi$ stacking interactions in the packing structure are the most important feature in **1**. As shown in Figure 3, the stacks of linear molecules **1** are slightly slipped along the packing direction. About one phenyl ring's shift is found between vicinal molecules forming the offset layer packing mode. The centroid–centroid distance between adjacent phenanthroline rings in a head-to-tail mode is 3.519 Å and that between one phenanthroline ring and one thiophene ring is 3.908 Å, exhibiting typical $\pi-\pi$ stacking interactions. Thus, an ordered 1D layer framework is constructed wherein all the alkyl chains are placed between the contiguous layers, which makes it a good candidate for research on semiconductor electronics. As far as we are aware, this is also the first single-crystal structural report on the 3,8-heterocycle-substituted phenanthroline compound (Cambridge Structural Database, Version 5.28).[13]

2.3. Characterizations of the Self-Assembled Films. Au-NPs with high activities were used in our experiments to facilitate the thiol-to-thiol ligand substitution between *tert*-dodecanethiol and dithiols **7**–**10**, which is a basic and key step for fabricating the self-assembled films. SEM images of the representative junctions are shown in Figure 4. The morphologies of the self-assembled nanocomposite films strongly rely on the number of ligands in the complexes and resulting geometric configurations in the presence of the same amount of Au-NPs. Parts a and b of Figure 4 show images of the self-assembled molecular junction **11** with different magnifications. The topography of this device is similar to those of oligothiophene-based dithiols because they have similar molecular structures.[9] However, no cracks can be observed in this junction, which may be related to the intrinsic properties of molecules during the formation of the self-assembled films. Figure 4c shows an SEM micrograph of junction **12** on the electrodes wherein the self-assembled film covers a wide region around the Au electrode pair. In this case, the film is much more homogeneous than in the case of **11** and oligothiophenes. Figure 4d shows an SEM micrograph with a resolution of 10 nm allowing for individual Au-NPs to be identified. The dark areas among the Au-NPs are supposed to be the dithiol molecules. It is suggested that the noncharged status of dithiol **11** and bivalent

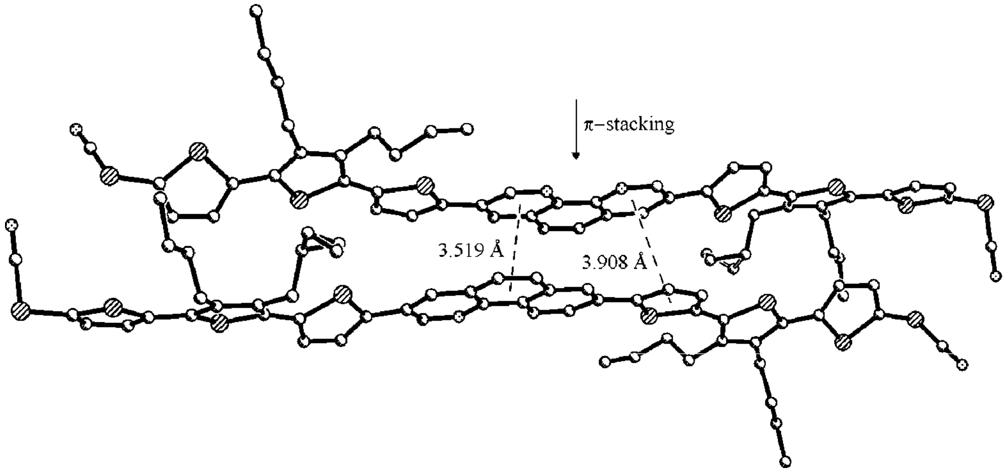

Figure 3. View of the $\pi-\pi$ stacking interactions in **1** with labeling of the centroid−centroid separations. Hydrogen atoms and solvent chloroform molecules are omitted for clarity.

$[Ru(bpy)]^{2+}$ cation **12** and their different steric effects are also responsible for the aggregation of dithiol-capped Au-NPs to a different extent. However, these images clearly show the formation of a granular self-assembled film between the microgap Au-electrodes although the oxidative oligomerization of dithiols, which is still one of the serious drawbacks of thiol chemistry, cannot be fully overcome.

The conformation and the concentration of the components are important factors for fabricating well-oriented and reproducible self-assembled films. On the one hand, with regard to the molecular junctions of **11**−**15**, the number of ligand **2** is increased from 1 to 2 or 3 and subsequently, active sites bonded with Au atoms are increased. Furthermore, the conformation of molecules has changed from quasilinear to quasispherical, which is defined by the coordination configurations of central transition metal ions. In this case, the deposition of the molecules has turned the growth process of the films into a three-dimensional one wherein aggregation of the molecules and the Au-NPs became quick. As can be seen in Figure 4e,f, for junctions of **13** and **14**, well-spread films could not be obtained due to aggregation of the molecules, but they prevail to form around the Au electrodes by means of Au−S bonds. In addition, the large amount of black precipitates emerging in the self-assembly process of **14** and **15** also verifies the quick aggregation process when the same concentration is used (see also the Supporting Information, Figure S1a−d). On the other hand, if the concentrations of the components are too high, well-oriented self-assembled films cannot be formed because of the quick cross-linkage and subsequent precipitation. At that time it is hard for the system to reach a kinetic stable state which is a crucial process in self-assembly. On the contrary, if the concentrations of the components are too low, the connection between two facing microgap gold electrodes cannot be guaranteed because there are not sufficient molecules. As a result, unstable *I*−*V* curves indicating low conductivity or no current will be present in the following experiments. In addition, stirring in the process of self-assembly is not recommended because it favors the aggregation process.

However, when a suitable concentration (0.5 mmol/L) was performed to fabricate nanodevices **12**, the reproducibility of the self-assembly process is good. Some additional SEM images are given as proof to verify the formation of well-oriented films including one image of a reference experiment where the Au-electrode without any gap was used and four images corresponding to two other nanodevices with different magnifications (see the Supporting Information, Figure S2a−e).

AFM studies provide further insight into the morphologies of these self-assembly thin films between the 1 μm gap Au-electrodes. Tapping mode AFM (TM-AFM) morphology (971 × 971 nm^2) of junction **12** illustrated in Figure 5 shows that the height variation (<10 nm) of the self-assembled film falls within the size of one free dithiol **7** stabilized Au-NP ($3.3 + 3.4 \times 2 = 10.1$ nm). This study shows that the Ru(II) dithiol, capped by two bpy molecules, may be the best candidate to prepare well-defined self-assembled films. All the SEM and AFM images verify the formation of self-assembled films bridging the microgap Au electrodes, which make it possible to determine the current−voltage (*I*−*V*) curves and photoresponse for the devices in this study.

2.4. Current−Voltage Characteristics of Self-Assembled Films for 11 and 12 in the Temperature Range of 8−300 K.

The devices prepared herein are very stable in air and are unchanged over a large range of bias voltage (up to −16 to 16 V) under repeated cycling. In our experiments, only the statistically average current can be recorded by the *I*−*V* monitor wherein a great number of molecules and Au-NPs contribute to the generation of the whole current between the 1 × 1 μm^2 gap areas. As a result, reproducible temperature-dependent *I*−*V* (measured current versus voltage) curves were recorded by using the cyclic scanning mode from 8 to 300 K with intervals of 20 K in the voltage range from −4 to 4 V with a step of 0.05 V. Furthermore, symmetric and fully overlapped *I*−*V* curves could be collected at negative and positive bias for all devices. Due to the severe aggregation in the cases of films **13**, **14**, and **15**, only the *I*−*V* characteristics and conduction mechanisms are intensively explored for relatively well-oriented junctions **11** and **12** to throw light on the effects of metal−ion complexation for the self-assembled films.

The full-range temperature-dependent (8−300 K) *I*−*V* curves of representative junctions of **11** and **12** fabricated under the same conditions are shown in Figure 6a and Figure 7a wherein L_2 and $[Ru(L_2)(bpy)_2]$ bridged Au-NPs serve as active elements. As can be seen in Figure 6a, the device *I*−*V* characteristics for **11** become increasingly nonlinear with decreasing temperature. At 300 K, the *I*−*V* curve is almost ohmic with resistance on the order of 9.95×10^7 ohm. The Arrhenius form of eq 1 is often used as a general formula to discuss the possible conduction mechanisms of the devices, which reflects the classical hopping transport of individual charges between the nearest neighboring particles. Classical Arrhenius plots (ln *I* versus 1/*T*) are used here to characterize the *I*−*V* behaviors of our devices (Figure 6b), from which at least two different mechanisms can be obtained. At low temperatures, the

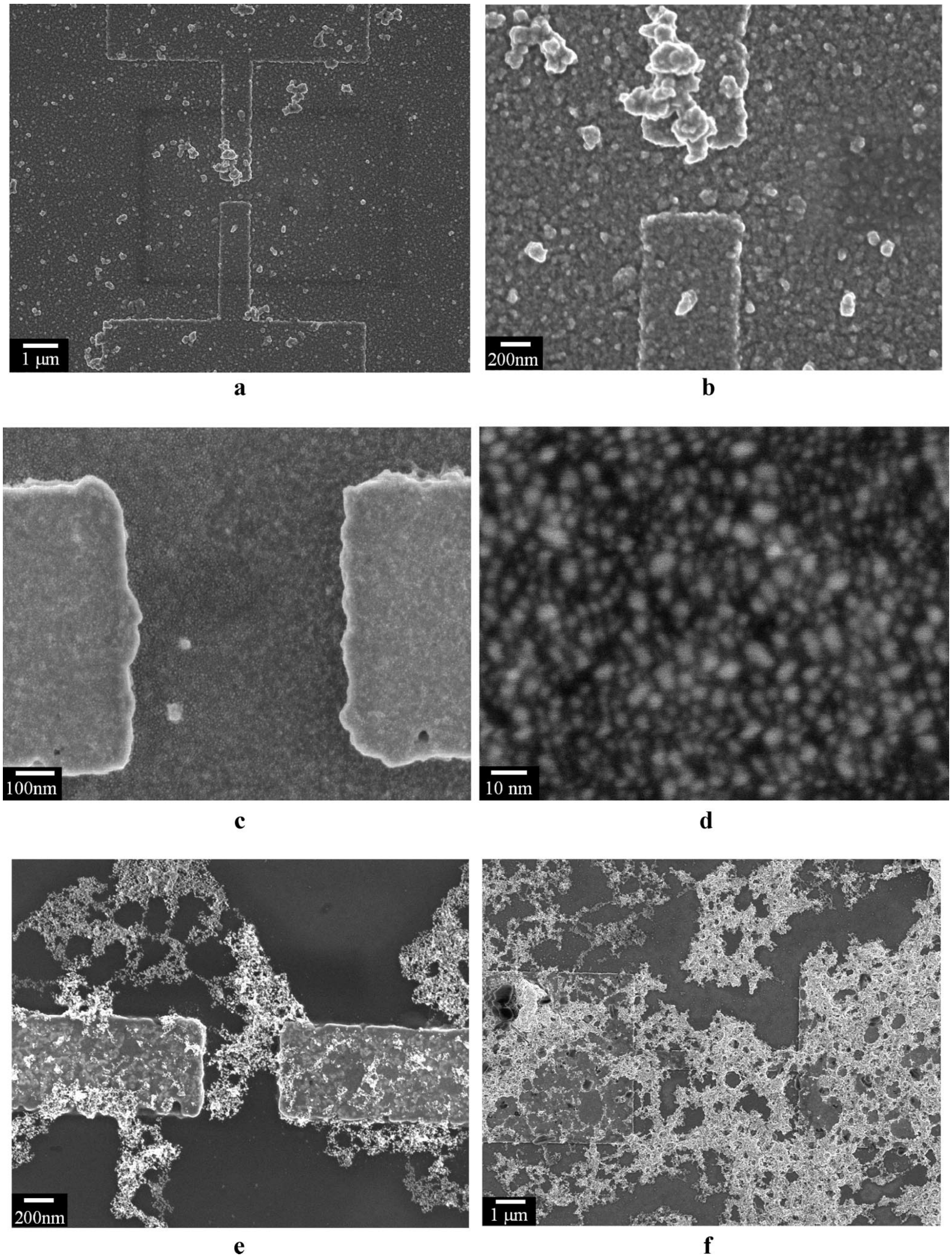

Figure 4. SEM images (top view) of self-assembled films covering the 1 × 1 μm^2 microgap of Au electrodes. (a and b) SEM images of one junction of **11** with different magnifications. (c and d) SEM images of one device of **12** on the gold electrodes with different magnifications. (e) SEM image of one junction of **13**. (f) SEM image of one junction of **14**.

currents are temperature independent since in this regime, the conductance is governed only by the tunneling between Au-NPs in the 1 × 1 μm^2 region. However, when the temperature increases, the contribution of the thermal excitation current, wherein thermally excited electrons hop from one isolated state to the next, the conductance of which depends strongly on the temperature, becomes dominant and will obscure the amount of the tunneling current. Since the tunneling current is temperature independent, one can deduct its contribution from the sum of the total current and obtain the Arrhenius plots again. When this is done, almost linear curves are obtained (Figure 6c) and the precise activation energy (ΔE) can be calculated by the theoretical fits for eight curves at different bias voltages, yielding an average $\Delta E = 13.2$ meV in the regimes of 40−300 K and 0.5−4 V for this device. The resulting intercept (b) for two films, corresponding to pre-exponential terms of the Arrhenius equation, is obviously different. For example, at 4 V, these values are −16.76 and −15.20 for nanocomposite films **11** and **12**, respectively, which may reflect the nature of nanocomposite films before and after metal−ion complexation. In addition, the differential intercept (Δb) of the fitted lines agrees well with $In(V_n + 0.5) - In(V_n)$ ($V_n = 0.5$, 1, 1.5, 2, 2.5, 3, and 3.5 V), corresponding to the mechanism of hopping conductance (eq 2).[14]

$$I \propto \exp\left[\frac{-\Delta E}{kBT}\right] \tag{1}$$

$$I \propto V \exp\left[\frac{-\Delta E}{kBT}\right] \tag{2}$$

$$I \propto V \exp\left[\frac{-4\pi d\sqrt{2m\Phi}}{h}\right] \qquad (3)$$

where V = applied voltage, I = current, T = temperature, m = electron mass, h = Planck's constant, k_B = Boltzmann constant, d = gap width, Φ = energy barrier for tunneling, and ΔE = activation energy for the film.

In comparison with **11**, the electronic conduction of nanodevice **12** increases when the Ru(II) ion is introduced into the system and all temperature-dependent $I-V$ curves are very close to linearity. At 300 K, the resistance is 1.55×10^7 ohm (Figure 7a), which is 15.6% of that of junction **11** at the same temperature. Classical Arrhenius plots also manifest the sum of contributions from the thermal and the tunneling conduction (Figure 7b). Hopping conduction with linear voltage dependent current also plays a key role at high temperature. A similar mathematical method was used to treat the data and the results yield the average barrier to injection $\Delta E = 12.1$ meV for **12** in the ranges of 40−300 K and 0.5−4 V (Figure 7c). The ΔE values of **11** and **12** are analogous to those extracted from oligothiophene dithiol-based devices prepared by the same method for which 7.3 and 16.0 meV were obtained in the cases of three and six thiophene rings, respectively.[9a]

Nevertheless, these ΔE values are less than the SAM junctions with ~100 meV activation energy at 0.1 V reported by Selzer et al.,[15] who used 1-nitro-2,5-di(phenylethynyl-4′-mercapto-)benzene in the absence of Au-NPs. Au-NPs dispersed in the films likely greatly reduced the activation energy barriers in our junctions. The ΔE values for device **11** and **12** are also smaller than those of octane-, dodecane- and hexadecanethiolate stabilized gold clusters (42, 104, and 156 meV) in the temperature range of 173−293 K,[16] mainly because monothiols are more weakly chemisorbed and long alkyl chain structures have a worse conjugated system compared with the aromatic-based dithiols we used. In addition, Schmid et al. also performed the relationship between ΔE and different bridging molecules by noncovalent bonds (95−260 meV).[17] By combing all these ΔE values, one can see some general structure-dependent conductivity for these molecular junctions, i.e., noncovalent contact, monothiol, long chain and alkyl molecules have higher ΔE values than covalent contact, dithiol, short chain and aromatic ones, and the use of Au-NPs can reduce the ΔE values of the clusters or films to some extent.

At 8 K, a linear $I-V$ relationship with resistance of 4.90×10^7 ohms is observed for junction **12** wherein Ru(II) is involved (R = 0.999 by performing the linear fit), which agrees well with the direct tunneling mechanism in the full voltage range (eq 3). Here, the ϕ_{DT} value is 200 meV (gap width d equals $3.36 + 0.25 \times 2$ nm) analogous to what Reed et al. have reported for a SAM molecular junction composed of a gold−sulfur−aryl−sulfur−gold system.[18] However, it is more complex for nanocomposite film **11**, where symmetric sigmoidal-shaped $I-V$ curves are obtained (Figure 8), which gives a correlation coefficient (R) of only 0.932 by performing a linear fit. In this case, direct tunneling cannot be used to explain the conducting mechanism and cotunneling may be responsible for this process.[19]

The difference in the observed resistance and the energy barrier for nanodevices **11** and **12** before and after the Ru(II)

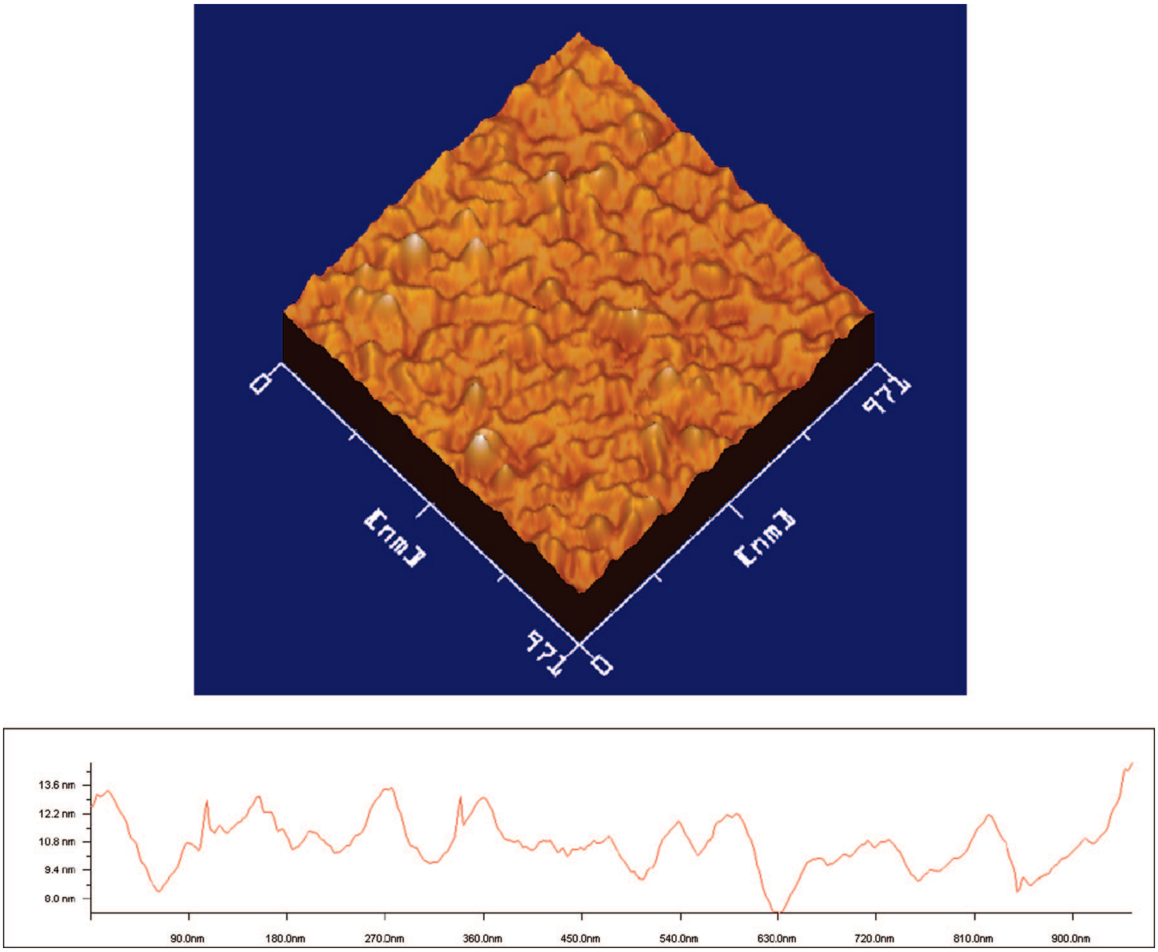

Figure 5. TM-AFM topography of the self-assembled film of **12** with an area of 971 × 971 nm^2.

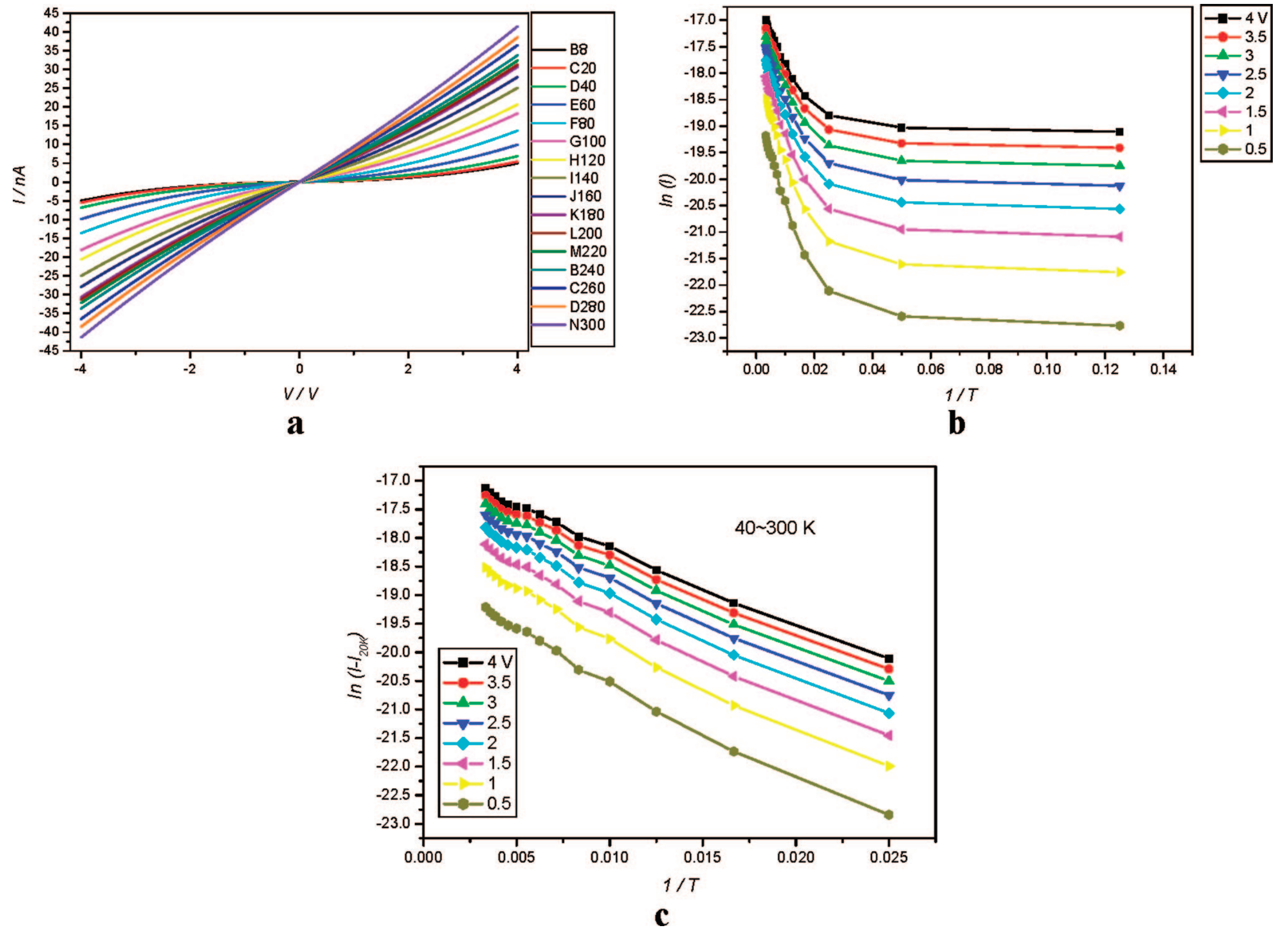

Figure 6. Temperature-dependent $I-V$ characteristics of the molecular junction **11**. (a) Full range of the $I-V$ curves (8−300 K, −4 to 4 V). (b) Arrhenius plots at 0.5−4 V in the range of 8−∼300 K. (c) Arrhenius plots for thermal excitation current only at 0.5−4 V in the range of 40−300 K.

ion complexation under the parallel experimental condition may be attributed to two factors. Namely, the change of highest occupied molecular orbital (HOMO) and lowest unoccupied molecular orbital (LUMO) gaps and permittivity of the surroundings around the nanoparticles of ligand and its Ru(II) complex, wherein the size of gold nanoparticles and the distance between the gold nanoparticles are very similar in nanodevices **11** and **12**.

Density Function Theory (DFT) computations are carried out with the Gaussian 03, Revision C.02 programs,[20] using the MPW1PW91 method and the LanL2DZ basis set. The fixed atom coordinates of **1** and **3**, based on the structural parameters of **1** determined by the X-ray diffraction method, are used for the HOMO−LUMO gap calculation. The resultant HOMO−LUMO gaps (band gaps) for ligand **1** and $[Ru(bpy)_2]^{2+}$ complex **3** are 2.864 and 1.569 eV, respectively. Compared with 4.149 and 2.614 eV for 3,8-bis(4-mercaptophenyl)-1,10-phenanthroline and its $[Ru(bpy)_2]^{2+}$ complex,[21] the band gaps are significantly reduced mainly due to the alteration of the π-conjugated system in different 3,8-substituted 1,10-phenanthroline ligands. So the introduction of Ru(II) ion into the system in this work plays a significant role in decreasing the band gaps of molecules, where the electron transportation between the HOMO and the LUMO of **3** can be greatly facilitated when excited.

Since the size of Au-NPs and the distance between the Au-NPs are very similar in nanocomposite films **11** and **12**, the influence of permittivity of nanoparticles should be taken into account in our temperature-dependent direct current determination. Here the permittivity of **12**/Au-NPs, composed of Ru(II) dication and two Cl^- counterions, is supposed to be much larger than that of neutral **11**/Au-NPs. Moreover, in view of a larger spatial crowding effect of $[Ru(bpy)]^{2+}$ complex **12** in comparison with that of **11**, fewer molecules can serve as bridges to link Au-NPs under the same experimental condition also leading to larger permittivity in the case of **12**/Au-NPs nanocomposite film. Since the charging energy of the nanoparticle, one of the important factors in determining the barriers to electron injection, heavily depends on the permittivity of the surroundings around the nanoparticles, the influence of the above-mentioned two factors in permittivity may facilitate the electron hopping between Au-NPs in the case of **12**/Au-NPs nanocomposite film. With the contribution of the above-mentioned decrease of band gap and increase of permittivity around the nanoparticles after the Ru(II) ion complexation under the parallel experimental condition, the observed resistance and average activation energy for nanodevice **12** are decreased.

A central issue and long-sought-after goal in the field of molecular electronics is the determination of the conductivity of a junction containing an individual molecule.[22] For a specific metal−molecule system, certain conduction mechanisms may dominate in certain voltage and temperature ranges and transport mechanisms are determined by the easiest conduction paths. In our case, at low temperature, tunneling current dominates the conduction for junctions **11** and **12**, whereas hopping conduction can satisfactorily explain the generation of the current when the temperature is increased, where the temperature-independent tunneling contribution is deducted. Dithiol ligand-passivated Au-NPs in the films are supposed to serve as the traps (or electron

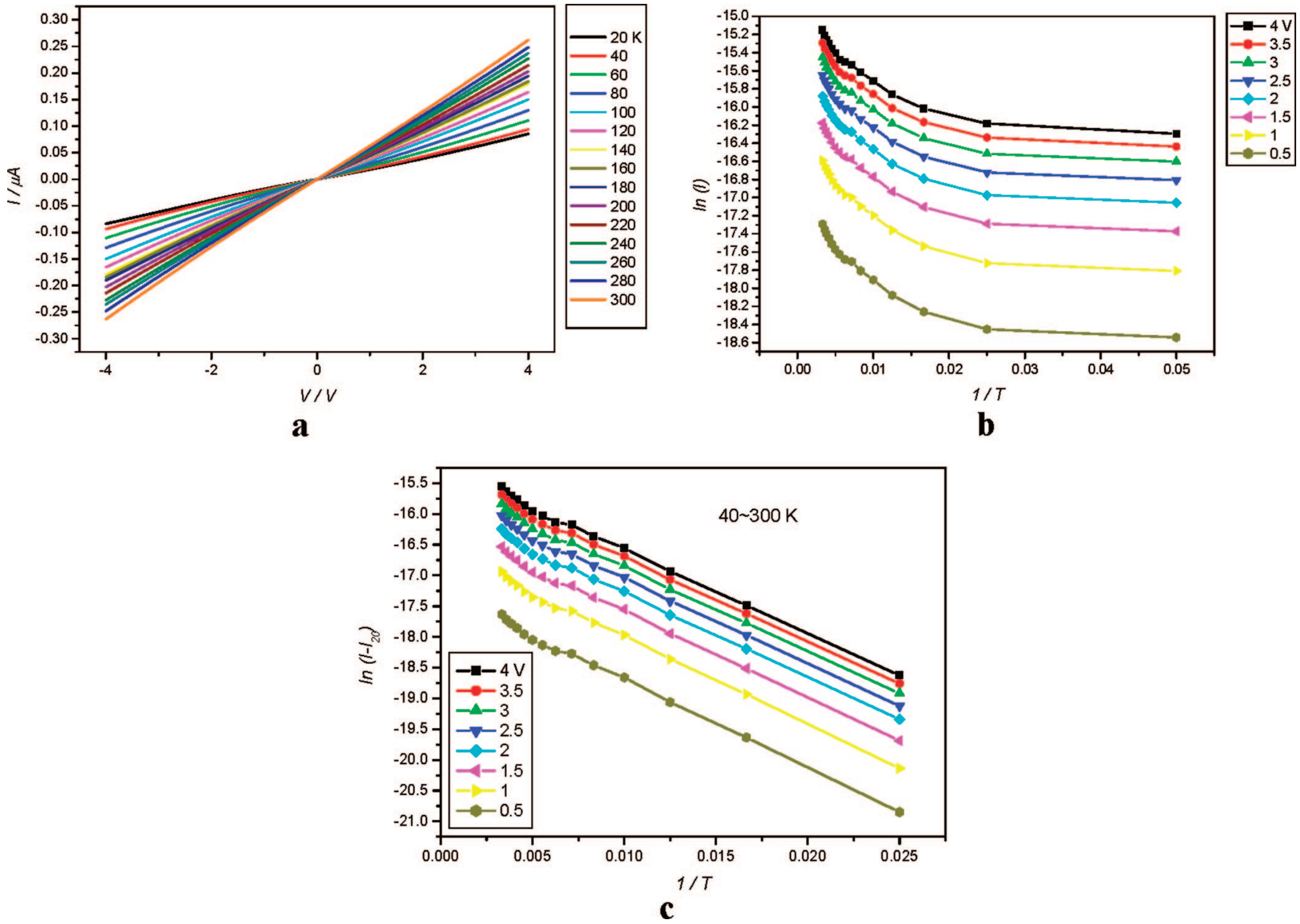

Figure 7. Temperature-dependent $I-V$ characteristics of one representative junction of **12**. (a) Full range of the $I-V$ curves (20−300 K). (b) Arrhenius plots at 0.5−4 V in the range of 8−300 K. (c) Arrhenius plots for thermal excitation current only at 0.5−4 V in the range of 40−300 K.

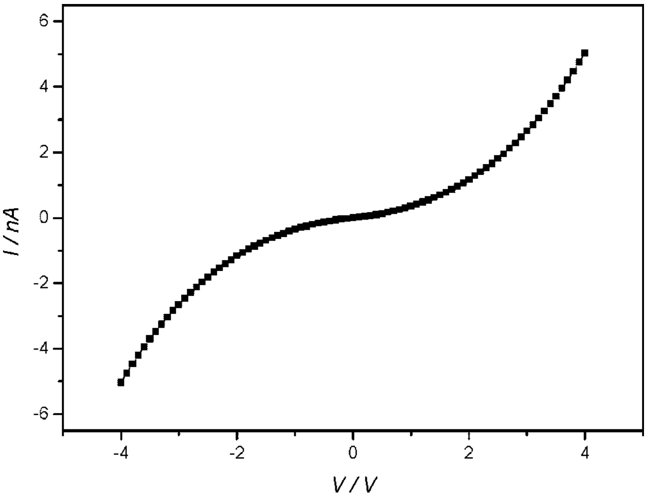

Figure 8. The measured $I-V$ curve at 8 K in a range from −4 to 4 V for nanodevice **11**.

pools, islands) to store, promote charge separation, and facilitate electron transportation among the molecules.[23,24]

2.5. Photoresponse Properties of Self-Assembled Films 11 and 12. The $I-V$ curves under irradiation for self-assembled films **11** and **12** were collected at 80, 160, and 300 K, and those in dark condition were also collected at the same temperature for comparison. The time−current scan mode with 0.5 s intervals was used at −3 or −6 V to record the process of the photoresponse, where the light source was switched periodically. When the strong light was irradiated onto the devices, the surface temperature would increase slightly first and then decrease quickly under the control of the effective thermostat (liquid helium coolant), where the temperature range varied only within 0.5 K. All the experiments were carried out at midnight in a dark room to minimize the influence of the surrounding light.

As can be seen in Figure 9, both the plots of voltage versus current and the plots of time versus current (the insets) exhibit reversible and reproducible photoresponsive for junction **11** at different temperature and bias voltage. Compared with the resistance in dark condition (black ones), the resistance of junction **11** at 80, 160, and 300 K is somewhat decreased under irradiation (red one) as a result of the photogeneration of charges making the substance more conductive, which means a photoactive film is present between the Au pair electrodes. However, analogous to the oligothiophene-based terminal dithiols/Au-NPs self-assembly films, the degree of photoresponse also relies on the temperature. Namely, lower temperature gives higher photoresponse and almost no obvious photoresponse can be observed at 300 K, which is suggested to be explained by their structural similarity.

From the $I-V$ and $I-T$ curves of nanodevice **12** with and without irradiation (Figure 10), one can clearly see the similar temperature-dependent photoresponse. However, the enhancement of photocurrent generation is observed after metal−ion complexation and the linear fits of light and dark $I-V$ graphs at 80, 160, and 300 K give the ratios of conductance ($K_{\text{light}}/K_{\text{dark}}$) at 1.44, 1.35, and 1.20, respectively. It is very interesting to mention that reversible room temperature photoresponse can

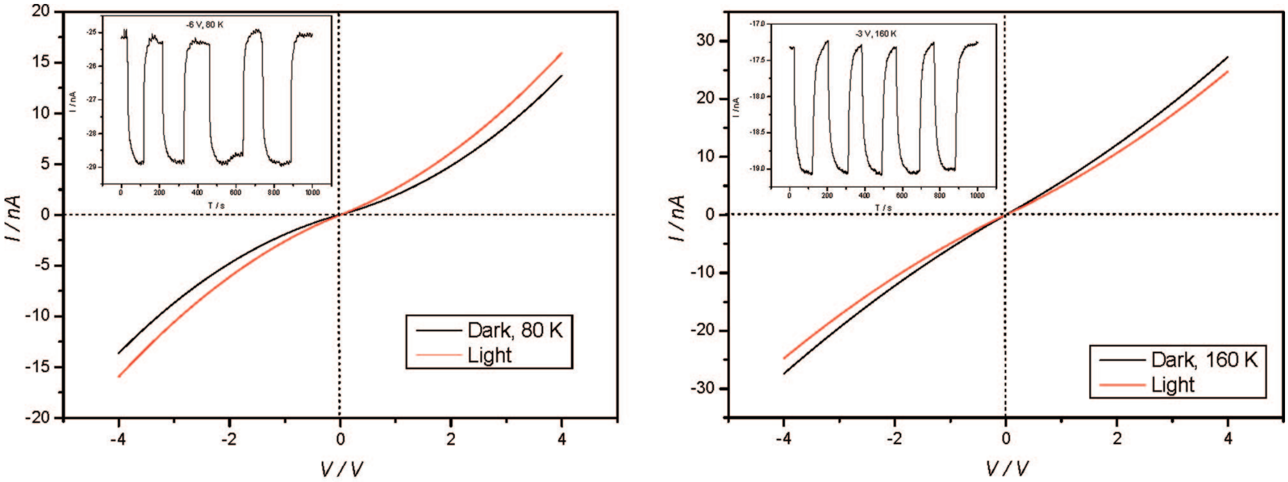

a (Inset: -6 V, 80 K) **b** (Inset: -3 V, 160 K)

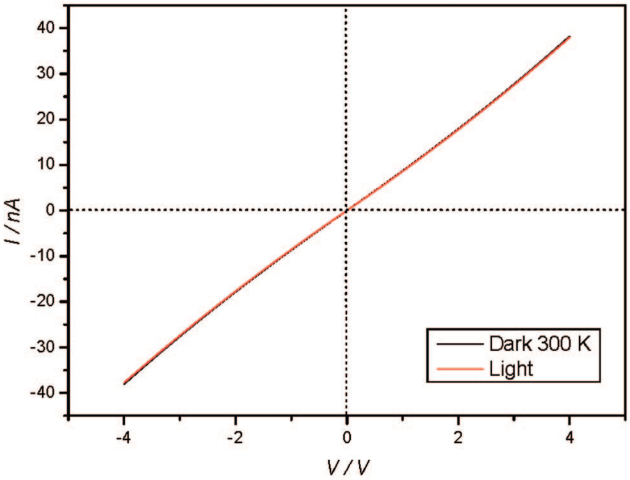

c

Figure 9. Reversible photoresponsive *I*−*V* and *I*−*T* curves of device **11**at different temperatures. (a) *I*−*V* curves under irradiation (red one) and in dark conditions (black one) in the range of −4 to 4 V at 80 K. The inset is the *I*−*T* curve when the light is turned on or off periodically at −6 V, 80 K. (b and c) *I*−*V* curves under irradiation (red one) and in dark condition (black one) in the range of −4 to 4 V at 160 and 300 K, respectively. The inset in panel b shows *I*−*T* curves when the light is turned on or off periodically at −3 V, 160 K.

be achieved, which may be a key step for the applications for these types of nanodevices such as photosensitive resistance and photosensitive diode.

Reversible and reproducible photoresponse can be observed for every nanodevice and little difference is observed from device to device in our experiments at 80, 160, and 300 K, where the ON/OFF ratios of current vary in a very small range (see the Supporting Information, Figure S3a−e for the *I*−*T* and *I*−*V* curves of another nanodevice **12**). The highest ratio of conductance ($K_{\text{light}}/K_{\text{dark}}$) obtained for junction **12** at 300 K in our experiments is 1.320 (see the Supporting Information, Figure S3f).

For the reason that Ru(II) complexes are one of the most frequently used photosensitizers because the $\text{Ru}^{\text{II}}/\text{Ru}^{\text{III}}$ single-electron oxidation process (MLCT) is relatively easy to achieve,[25] the introduction of Ru(II) species into the system may help to stabilize the oligothiophenium cation of the ligand[26] (the first oxidation state having a much better conductivity) under irradiation. So the enhancement of photoresponse is expected in our Au-NPs/dithiols self-assembly films after the metal−ion complexation and room temperature photoresponse can be observed.

3. Conclusions

In summary, the first single-crystal structure of 3,8-heterocycle-disubstituted phenanthroline compound (**1**) with a molecular length of 3.36 nm was described, and was used as a precursor for preparing the corresponding terminal dithiol. Self-assembled nanocomposite films were derived from this terminal dithiol and its transition metal coordination complexes [Ru(II), Fe(II), and Cu(II)], with different numbers of dithiol groups in the molecules to reveal the effects of metal−ion complexation. The morphologies of these films are obviously different due to the alteration of the molecular conformation by the introduction of different kinds of center metal cations and counterions, as demonstrated by their SEM and AFM images.

These films also manifest typical temperature-dependent semiconductor *I*−*V* behaviors in the range of 8−300 K. Quantitative measurements are carried out on the conductance and photoresponse of self-assembled films containing Au-NPs and terminal dithiols in similar sizes and the comparisons on the effects of metal−ion complexation, which are fundamental issues in the emerging area of molecular-scale electronics. The current generation in all devices at different temperatures is dominated by a combination of tunneling and thermal excitation

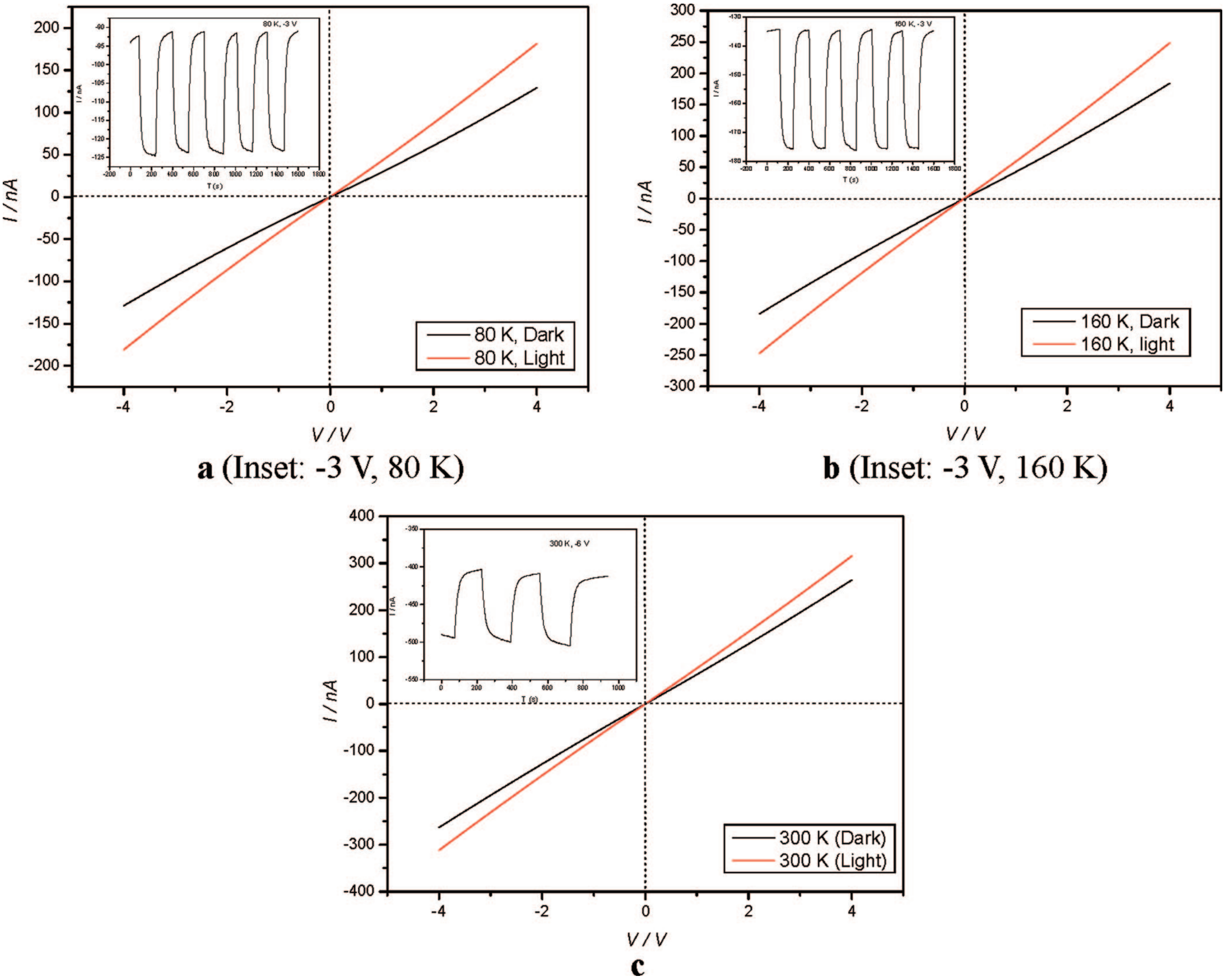

a (Inset: -3 V, 80 K)

b (Inset: -3 V, 160 K)

c

Figure 10. Reversible photoresponsive *I*−*V* and *I*−*T* curves of nanodevice **12**. (a) *I*−*V* curves under irradiation (red one) and in dark conditions (black one) in the range of −4 to 4 V at 80 K. The inset shows the *I*−*T* curve when the light is turned on or off periodically at −3 V, 80 K. (b and c) *I*−*V* curves under irradiation (red one) and in dark condition (black one) in the range of −4 to 4 V at 160 and 300 K, respectively. The insets are *I*−*T* curves when the light is turned on or off periodically at −3 V, 160 and −6 V, 300 K, respectively. (Inset: −6 V, 300 K).

mechanisms. When the temperature-independent tunneling current was subtracted from the overall current, the conductance of the devices follows the classical Arrhenius equation from which the average activation energies (ΔE) in specific voltage ranges for each device can be obtained by linear fits.

More interestingly, photoresponsive studies for these films reveal that they are optically active and the generation of photocurrent can be enhanced after the metal−ion complexation, wherein reversible and reproducible photoresponse at room temperature can be recorded. In contrast, only low-temperature photoresponse can be observed for the self-assembled films composed of Au-NPs and 3,8-bis(terthiophenyl)phenanthroline dithiol ligand, which is similar to our previously reported oligothiophene dithiols/Au-NPs junctions.

This kind of work is interesting because the incorporation of ligands and corresponding metal complexes in a π-conjugated structure allows the fine-tuning of important physical properties, especially for redox behavior or photophysical properties. According to our work, it is supposed that the introduction of $[Ru(bpy)_2]^{2+}$ species into the system improves the morphology by decreasing the defects of the resulting self-assembled film, decreases the band gap of molecule, increases the permittivity around the gold nanoparticles under the parallel experimental condition, and hence increases the overall conductivity and decreases the barriers for activation energy of nanocomposite film **12**. More importantly, compared with the ligand itself as well as our previously studied oligothiophenes, photosensitivity is enhanced after the metal−ion complexation. The possible reason may come from the change of the band gap, which can be verified by DFT calculations and the presence of MLCT under light irradiation when the transition metal ion is introduced, which may help to stabilize the oligothiophenium cation of the ligand (the first oxidation state having a much better conductivity). Further studies are underway on the influence of the transformation of redox states on conductivity, wavelength dependent photoresponse, and Kelvin probe force microscopy for these molecular junctions before and after metal−ion complexation.

4. Experimental Section

4.1. Materials and Measurements. All reagents and solvents used were of analytical grade and were used without further purification. The anhydrous solvents were drawn into a syringe under a flow of dry N_2 gas and were directly transferred into the reaction flask to avoid contamination. $[Fe(pyridine)_4(NCS)_2]$ was prepared and purified as yellow powder with a yield of

TABLE 1: Crystal and Refinement Data for Compound 1

compd no.	**1**
empirical formula	$C_{55}H_{51}N_4S_8Cl_3$
formula weight	1130.83
crystal size, mm^3	0.40 × 0.20 × 0.10
crystal system	triclinic
space group	$P\bar{1}$ (no. 2)
a, Å	13.388(3)
b, Å	13.833(3)
c, Å	16.353(3)
α, deg	80.08(3)
β, deg	80.02(3)
γ, deg	65.63(3)
V, Å^3	2699.7(10)
Z; D_{calcd}, Mg/m^3	2; 1.391
F(000)	1176
μ, mm^{-1}	0.521
wavelength, Å	0.71073
T, K	100(2)
total, unique data, R_{int}	23585, 9401, 0.075
no. of observations [$I > 2\sigma(I)$]	7952
no. of parameters	644
refinement method	full-matrix least-squares on F^2
absorption correction	multiscan
h_{min}/h_{max}	−15/14
k_{min}/k_{max}	−16/16
l_{min}/l_{max}	−19/18
final R indices [$I > 2\sigma(I)$]^a	$R_1 = 0.0748$, $wR_2 = 0.1647$
R indices (all data)^a	$R_1 = 0.0936$, $wR_2 = 0.1738$
GOF on F^2	1.133
△ (max, min), e·Å^{-3}	0.663, −0.533

[a] $R_1 = \sum||F_o| - |F_c||/\sum|F_o|$, $wR_2 = \{\sum[w(F_o^2 - F_c^2)^2]/\sum w(F_o^2)^2\}^{1/2}$.

TABLE 2: Selected Bond Distances (Å) and Angles (deg) for 1

bond distances		bond angles	
S1−C13	1.729(5)	C13−S1−C16	92.8(2)
S1−C16	1.735(5)	C17−S2−C20	92.5(2)
S2−C20	1.733(5)	C21−S3−C24	91.8(2)
S2−C17	1.734(5)	C24−S4−C25	101.2(3)
S3−C24	1.719(5)	C34−S5−C37	92.9(2)
S3−C21	1.735(5)	C38−S6−C41	92.0(2)
S4−C24	1.759(6)	C42−S7−C45	91.9(2)
S4−C25	1.655(8)	C45−S8−C46	99.1(2)
S5−C37	1.727(4)	S4−C25−N4	178.1(8)
S5−C34	1.732(5)	S8−C46−N3	179.0(5)
S6−C38	1.732(5)		
S6−C41	1.731(5)		
S7−C42	1.735(5)		
S7−C45	1.722(5)		
S8−C46	1.692(5)		
S8−C45	1.765(5)		
N1−C10	1.326(6)		
N1−C11	1.362(6)		
N2−C1	1.320(6)		
N2−C12	1.362(6)		
N3−C46	1.142(7)		
N4−C25	1.153(12)		
C2−C13	1.466(6)		
C4−C12	1.408(7)		
C9−C34	1.453(6)		
C16−C17	1.456(6)		
C20−C21	1.454(6)		
Cl1−C55	1.767(6)		
Cl2−C55	1.755(5)		
Cl3−C55	1.749(6)		

75% via a method previously reported by Erickson and Sutin.[27] The intermediates and products were characterized by elemental analysis and spectroscopic methods. *tert*-Dodecanethiol-protected active Au-NPs were prepared by using a modified Brust Method.[28] Gold nanoelectrodes with 1 μm gaps were prepared by a method described previously.[9a] Each 3 × 3 mm^2 silicon chip was thoroughly washed with toluene, acetone, and methanol, then cleaned in an oxygen plasma asher prior to SEM analysis. For the preparation for self-assembled films with *tert*-dodecanethiol-protected active Au-NPs in $CHCl_3$, the electrodes with 1 μm gaps were cleaned carefully in CF_4 plasma and checked with an optical microscopy prior to use.

Caution: Although no problem was encountered in all our experiments, transition-metal perchlorates are potentially explosive and should be handled in small quantities.

UV−vis spectra were recorded with a Shimadzu UV-3150 double-beam spectrophotometer, using a Pyrex cell with a path length of 10 mm at room temperature. Infrared spectra (4000−400 cm^{-1}) were recorded with a Horiba FT-700 spectrophotometer. FAB-MS spectra were measured with a JEOL JMS-777V spectrometer. An OLYMPUS BX60 M optical microscope was used to check all the electrodes before determination of $I-V$ curves. A Yanaco PLASMA ASHER LTA-102 instrument was used to clean all the electrodes. Scanning electron microscope (SEM) images were collected with a JEOL JSM-6700F microscope with an acceleration voltage of 3 KV. Atomic Force Microscope (AFM) images were recorded on a JEOL-JSPM4210 instrument. The measurement is carried out in vacuum to eliminate the influence of water adsorbed on the sample surface and increase the sensitivity and reproducibility of the experiment. The resonant frequency of the cantilevers was 250 kHz for tapping mode. The light source used for irradiating the samples with the maximum intensity is a NPI PCS-UMX250 High Power Metal Halide Lamp.

The $I-V$ curves were collected with an Advantest R6245 2-Channel Voltage Current Source Monitor interfaced with a microcomputer through a GPIB-SCSI board and NI-488.2 protocol. Data were acquired with use of a homemade procedure and Igor Pro 4.0 (Wavemetrics) software. The samples were mounted on the top of an antivibration table with a temperature-controlled cryogenic chamber (±0.005 °C). All measurements were carried out in high vacuum ($P < 2.0 \times 10^{-4}$ Pascal) formed by means of a turbomolecular pump, and the samples were cooled by using liquid helium as the coolant (5 to 300 K). Triaxial cables were used to connect the molecular devices and the $I-V$ monitor to minimize external noise.

4.2. X-ray Data Collection and Solution. A single-crystal sample of 3,8-bis(3′,4′-dibutyl-5″-thiocyanato-2,2′:5′,2″-terthiophen-5-yl)-1,10-phenanthroline (**1**) was covered with glue and mounted on a glass fiber, and then used for data collection on a Rigaku Mercury CCD area-detector at 100(2) K, using graphite monochromated Mo Kα radiation ($\lambda = 0.71073$ Å). The diffraction data thus collected were reduced by using the program Crystalclear[29] and empirical absorption corrections were performed. The original data files generated by Crystalclear were transformed to SHELXTL97 format by the TEXSAN program,[30] and then the structure was solved by direct methods and refined by a least-squares method on F_{obs}^2 by using the SHELXTL-PC software package.[31] All non-H atoms were anisotropically refined and all hydrogen atoms were inserted in the calculated positions (C−H, 0.96 Å) assigned fixed isotropic thermal parameters at 1.2 times the equivalent isotropic U of the atoms to which they are attached (1.5 times for the methyl groups), and allowed to ride on their respective parent atoms. All calculations and molecular graphics were carried out with the SHELXTL PC program package on a personal computer. A summary of the crystal data, experimental details, and

SCHEME 2: Schematic Illustration for the Preparation of the Compounds and Self-Assembled Thin Films

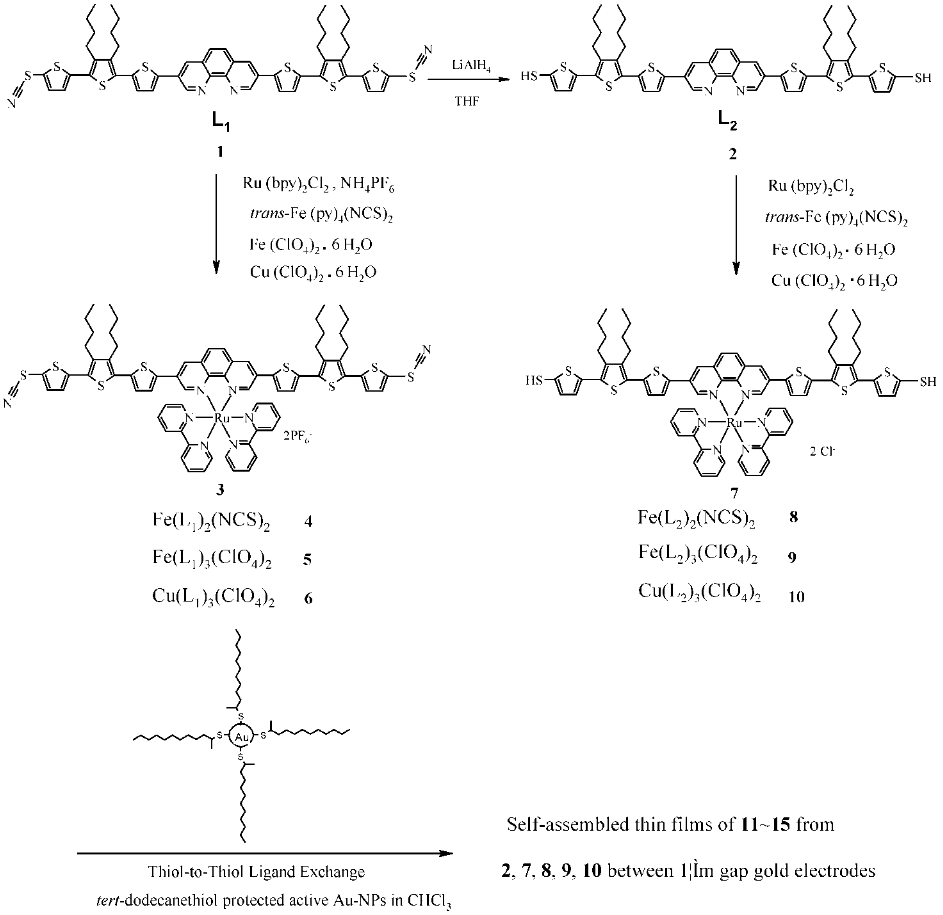

refinement results is listed in Table 1, while selected bond distances and bond angles are given in Table 2.

4.3. Preparation of Compounds 1 and 3. Synthesis of **1** and bis(2,2′-bipyridyl)(3,8-bis(3′,4′-dibutyl-5″-thiocyanato-2,2′:5′,2″-terthiophen-5-yl)-1,10-phenanthroline)ruthenium(II) hexafluorophosphorate ([Ru(bpy)$_2$(L$_1$)](PF$_6$)$_2$, **3**) was carried out by means of the method we described previously.[11] A single-crystal sample of **1** suitable for X-ray diffraction determination was grown from a mixed solution of chloroform and acetone (2:1, v/v) by slow evaporation in air at room temperature.

***Synthesis of Compound* 2.** The method is essentially the same as the preparation of oligothiophenes we described previously.[9a] A suspension of LiAlH$_4$ (0.10 g, 2.6 mmol) in dry THF (20 cm^3) in N$_2$ atmosphere in a three-necked round-bottomed flask equipped with a condenser was added carefully to a solution of **1** (0.50 g, 0.50 mmol) in dry THF (30 cm^3) at room temperature. The mixture was stirred for 2 h at room temperature, quenched with 1 mol/L of hydrochloric acid, and then poured into 50 cm^3 of chloroform. The organic layer was washed thoroughly with distilled water and dried with anhydrous Na$_2$SO$_4$. The solvents were removed by a rotatory evaporator and the red residue was dried in vacuum. The yield was 0.44 g (92%). The resulting yellow solids were used instantly for the next synthesis without any purification because the LiAlH$_4$ reduction is almost quantitative (yields >90%) and the dithiol **2** is very sensitive to oxygen. ^{1}H NMR (500 MHz, CDCl$_3$) δ 9.43 (d, $J = 1.5$ Hz, 2H, phen), 8.40 (d, $J = 2.5$ Hz, 2H, phen), 7.89 (s, 2H, phen), 7.54 (d, $J = 3.4$ Hz, 2H, thiophene), 7.47 (d, 2H, $J = 2.4$ Hz, thiophene), 7.29 (d, 2H, $J = 2.5$ Hz, thiophene), 7.05 (d, 2H, $J = 1.5$ Hz, thiophene), 3.74 (s, 2H, thiol), 2.79 (m, 8H, alkyl), 1.60−1.29 (m, 16H, alkyl), 0.96 (t, 6H, alkyl), 0.88 (t, 6H, alkyl). Main FT-IR (KBr pellets, ν, cm^{-1}) 2925 (m), 1654 (m), 1560 (m), 1542 (m), 1458 (m), 1376 (m), 1090 (s), 913 (s), 744 (s). Elemental Anal. Calcd for C$_{52}$H$_{52}$N$_2$S$_8$: C, 64.96; H, 5.45; N, 2.91. Found: C, 64.99; H, 5.58; N, 2.83. FAB-MS: *m/z* 961 (M$^+$).

Synthesis of [Fe(L$_1$)$_2$(NCS)$_2$] (4). A 20 cm^3 chloroform solution of **1a** [Fe(pyridine)$_4$(NCS)$_2$] (0.122 g, 0.25 mmol) was added to 2-fold of **1** (0.50 g, 0.50 mmol) dissolved in 20 cm^3 of chloroform, and the mixture was then stirred for 1 h in a glovebox. The mixture was filtered and 50 cm^3 of methanol was added to the filtrate. Red precipitates were collected with a yield of 82%. Main FT-IR (KBr pellets, ν, cm^{-1}): 3432 (br), 3073 (w), 2953 (s), 2929 (s), 2868 (m), 2157 (m), 2111 (s), 2088 (vs), 2051 (s), 1600 (s), 1440 (s), 1379 (m), 1282 (w), 1082 (s), 914 (m), 802 (s), 720 (w) cm^{-1}. Elemental Anal. Calcd for [Fe(L$_1$)$_2$(NCS)$_2$]·2H$_2$O: C, 60.75, H, 4.79, N, 6.05, S, 25.71. Found: C, 60.69, H, 4.85, N, 6.08, S, 25.69. FAB-MS: *m/z*: 2136 [Fe(L$_1$)$_2$(NCS)]$^+$. UV−vis (λ_{max}) in CH$_2$Cl$_2$: 365 and 448 nm.

Synthesis of [Fe(L$_1$)$_3$](ClO$_4$)$_2$ (5). Treatment of 3 equiv of **1** (0.75 g, 0.75 mmol) dissolved in 30 cm^3 of chloroform with Fe(ClO$_4$)$_2$·6H$_2$O (0.91 g, 0.25 mmol) dissolved in 10 cm^3 of acetone yielded **5** with a high yield of 86% at room temperature. Main FT-IR (KBr pellets, ν, cm^{-1}): 3448 (br), 3074 (w), 2955 (s), 2929 (s), 2868 (m), 2157 (m), 1597 (s), 1459 (s), 1440 (s), 1380 (m), 1281 (w), 1104 (vs), 1099 (vs), 906 (m), 804 (s), 720 (w), 622 (m) cm^{-1}. Elemental Anal. Calcd for [Fe(L$_1$)$_3$](ClO$_4$)$_2$·4H$_2$O: C, 57.88, H, 4.74, N, 5.00, S, 22.89. Found: C, 57.71, H, 4.72, N, 5.06, S, 22.84. FAB-MS: *m/z* 3189 [Fe(L$_1$)$_3$ClO$_4$]$^+$. UV−vis (λ_{max}) in CH$_2$Cl$_2$: 356 and 475 nm.

Synthesis of [Cu(L$_1$)$_3$](ClO$_4$)$_2$ (6). Treatment of 3-fold of **1** (0.75 g, 0.75 mmol) dissolved in 30 cm^3 of chloroform with $Cu(ClO_4)_2 \cdot 6H_2O$ (0.93 g, 0.25 mmol) dissolved in 10 cm^3 of acetone yielded **6** with a high yield of 88% at room temperature. Main FT-IR (KBr pellets, ν, cm^{-1}): 3422 (br), 3074 (w), 2954 (m), 2926 (s), 2868 (w) 2157 (m), 1654 (m), 1599 (s), 1459 (s), 1440 (s), 1381 (m), 1105 (vs), 1087 (vs), 720 (m), 622 (w). Elemental Anal. Calcd for $[Cu(L_1)_3](ClO_4)_2 \cdot 2H_2O$: C, 58.38, H, 4.66, N, 5.04, S, 23.09. Found: C, 58.37, H, 4.70, N, 5.07, S, 23.06. FAB-MS: *m/z* 3197 $[Cu(L_1)_3ClO_4]^+$. UV−vis (λ_{max}) in CH_2Cl_2: 359 and 469 nm.

***Syntheses of Complexes* 7, 8, 9, *and* 10.** The syntheses of **7**, **8**, **9**, and **10** were performed with a similar method to the above. The chloroform solutions of **2** were added to an equal molar ratio of methanol solutions of $Ru(bpy)_2Cl_2$, $[Fe(py)_4(NCS)_2]$, $Fe(ClO_4)_2 \cdot 6H_2O$, and $Cu(ClO_4)_2 \cdot 6H_2O$, respectively. The mixtures were stirred at room temperature under a N_2 atmosphere and the color changed from yellow to red. The complexes were not isolated and were used directly in the next self-assembly; however, they were determined by ESI-MS to verify the complexation. ESI-MS: *m/z* **7**, 1410 $[Ru(L_2)(bpy)_2Cl]^+$; **8**, 2037, $[Fe(L_2)_2(NCS)]^+$; **9**, 3040, $[Fe(L_2)_3(ClO_4)]^+$; **10**, 3048, $[Cu(L_2)_3(ClO_4)]^+$.

Preparation of Self-Assembled Films of* 11−15 *on 1 μm Gap Au Electrodes. The junctions were fabricated by the self-assembly method illustrated in Scheme 2. Freshly cleaned gold electrodes with a ∼1 μm gap and a ∼1 μm width were soaked in chloroform solutions of **2**, **7**, **8**, **9**, and **10** (0.5 mmol/L with respect to the dithiol) for 30 min, respectively, and then a chloroform solution of *tert*-dodecanethiol-protected active Au-NPs (0.5 mmol/L) was added. The mixtures were kept standing for 16 h at room temperature in a glovebox. The electrodes were then taken out, washed thoroughly with chloroform to remove excess unreacted Au-Nps and dithiols, and dried in a vacuum.

Acknowledgment. This work was supported by a Grant-in-Aid for Scientific Research (Nos. 15201028 and 14654135) and for Key-Technology, “Atomic Switch Programmed Device” from the Ministry of Culture, Education, Science Sports, and Technology of Japan. W.H. would like to acknowledge the Major State Basic Research Development Programs (Nos. 2007CB925101 and 2006CB806104) and the National Natural Science Foundation of China (Nos. 20721002 and 20301009).

Supporting Information Available: SEM images of junctions **13**, **14**, and **15** with 4 or 6 thiol groups in their molecular structures to show the aggregation of molecules during the self-assembly process, SEM images of three other devices for junction **12** and reversible photoresponsive *I-T* and *I−V* curves of another nanodevice **12** at 80, 160, and 300 K. This material is available free of charge via the Internet at http://pubs.acs.org. CCDC reference number 285471 contains supplementary crystallographic data to the data presented in this paper; these data can be obtained free of charge at www.ccdc.cam.ac.uk/conts/retrieving.html [or from the Cambridge Crystallographic Data Centre, 12, Union Road, Cambridge CB2 1EZ, UK; Fax: (International) +44-1223/336-033; e-mail deposit@ccdc.cam.ac.uk].

References and Notes

(1) Schmid, G. *Nanoparticles: From theory to application*; WILEY-VCH Verlag GmbH & Co. KGaA: Weinheim, Germany, 2004.

(2) (a) Collier, C. P.; Vossmeyer, T.; Heath, J. R. *Annu. Rev. Phys. Chem.* **1998**, *49*, 371–404. (b) Schmid, G.; Baumle, M.; Geerkens, M.; Helm, I. *Chem. Soc. Rev.* **1999**, *28*, 179–185. (c) Murray, C. B.; Kagan, C. R.; Bawendi, M. G. *Annu. Rev. Mater. Sci.* **2000**, *30*, 545–610. (d) Klimov, V. I.; Mikhailovsky, A. A.; Xu, S.; Malko, A.; Hollingsworth, J. A.; Leatherdale, C. A.; Eisler, H. J.; Bawendi, M. G. *Science* **2000**, *290*, 314–317.

(3) (a) Murray, C. B.; Kagan, C. R.; Bawendi, M. G. *Science* **1995**, *270*, 1335–1338. (b) Schlenoff, J. B.; Li, M.; Ly, H. *J. Am. Chem. Soc.* **1995**, *117*, 12528–12536. (c) Ovchenkov, Y. A.; Geisler, H.; Burst, J. M.; Thornburg, S. N.; Ventrice, C. A.; Zhang, C. J.; Redepenning, J.; Losovyj, Y.; Rosa, L.; Dowben, P. A.; Doudin, B. *Chem. Phys. Lett.* **2003**, *381*, 7–13. (d) Kanehara, M.; Oumi, Y.; Sano, T.; Teranishi, T. *J. Am. Chem. Soc.* **2003**, *125*, 8708–8709. (e) Speets, E. A.; Ravoo, B. J.; Roesthuis, F. J. G.; Vroegindeweij, F.; Blank, D. H. A.; Reinhoudt, D. N. *Nano Lett.* **2004**, *4*, 841–844. (f) Xu, D. W.; Graugnard, E.; King, J. S.; Zhong, L. W.; Summers, C. J. *Nano Lett.* **2004**, *4*, 2223–2226. (g) Ashwell, G. J.; Berry, M. *J. Mater. Chem.* **2005**, *15*, 108–110.

(4) (a) Teranishi, T.; Haga, M.; Shiozawa, Y.; Miyake, M. *J. Am. Chem. Soc.* **2000**, *122*, 4237–4238. (b) Zamborini, F. P.; Hicks, J. F.; Murray, R. W. *J. Am. Chem. Soc.* **2000**, *122*, 4514–4515. (c) Ogawa, T.; Kobayashi, K.; Masuda, G.; Takase, T.; Maeda, S. *Thin Solid Films* **2001**, *393*, 374–378. (d) Beverly, K. C.; Sample, J. L.; Sampaio, J. F.; Remacle, F.; Heath, J. R.; Levine, R. D. *Proc. Natl. Acad. Sci. U.S.A.* **2002**, *99*, 6456–6459. (e) Beverly, K. C.; Sampaio, J. F.; Heath, J. R. *J. Phys. Chem. B* **2002**, *106*, 2131–2135. (f) Remacle, F.; Beverly, K. C.; Heath, J. R.; Levine, R. D. *J. Phys. Chem. B* **2002**, *106*, 4116–4126. (g) Remacle, F.; Levine, R. D. *Nano Lett.* **2002**, *2*, 697–701. (h) Brennan, J. L.; Branham, M. R.; Hicks, J. F.; Osissek, A. J.; Donkers, R. L.; Georganopoulou, D. G.; Murray, R. W. *Anal. Chem.* **2004**, *76*, 5611–5619. (i) Minamoto, M.; Matsushita, M.; Sugawara, T. *Polyhedron* **2005**, *24*, 2263–2268. (j) Zhao, W.; Xu, J. J.; Shi, C. G.; Chen, H. Y. *Langmuir* **2005**, *21*, 9630–9634. (k) Lim, I. I. S.; Goroleski, F.; Mott, D.; Kariuki, N.; Ip, W.; Luo, J.; Zhong, C. J. *J. Phys. Chem. B* **2006**, *110*, 6673–6682. (l) Ozawa, H.; Kawao, M.; Tanaka, H.; Ogawa, T. *Langmuir* **2007**, *23*, 6365–6371.

(5) Petty, M. C. ; Bryce, M. R. ; Bloor, D. *Introduction to Molecular Electronics*; Oxford University Press: New York, 1995.

(6) See, for recent reviews:(a) Metzger, R. M. *Chem. Rev.* **2003**, *103*, 3803–3834. (b) James, D. K.; Tour, J. M. *Chem. Mater.* **2004**, *16*, 4423–4435. (c) McCreery, R. L. *Chem. Mater.* **2004**, *16*, 4477–4496.

(7) (a) Koezuka, H.; Tsumura, A.; Fuchigami, H.; Kumamoto, K. *Appl. Phys. Lett.* **1993**, *62*, 1794–1796. (b) Garnier, F.; Hajlaoui, R.; Yassar, A.; Srivastava, P. *Science* **1994**, *265*, 1684–1686. (c) Dodabalapur, A.; Torsi, L.; Katz, H. E. *Science* **1995**, *268*, 270–271. (d) Dodabalapur, A.; Katz, H. E.; Torsi, L.; Haddon, R. C. *Science* **1995**, *269*, 1560–1562.

(8) Bradley, D. D. C. *Synth. Met.* **1993**, *54*, 401–415.

(9) (a) Huang, W.; Masuda, G.; Maeda, S.; Tanaka, H.; Ogawa, T. *Chem. Eur. J.* **2006**, *12*, 607–619. (b) Ogawa, T.; Huang, W.; Tanaka, H. *Mol. Cryst. Liq. Cryst.* **2006**, *455*, 299–303.

(10) Nakamoto, K. *Infrared and Raman Spectra of Inorganic and Coordination Compounds*, 3rd ed.; John Wiley & Sons: New York, 1978.

(11) Araki, K.; Endo, H.; Masuda, G.; Ogawa, T. *Chem. Eur. J.* **2004**, *10*, 3331–3340.

(12) Juris, A.; Balzani, V.; Barigelletti, F.; Campagna, S.; Belser, P.; von Zelewsky, A. *Coord. Chem. Rev.* **1988**, *84*, 85–277.

(13) Allen, F. H. *Acta Crystallogr., Sect. B* **2002**, *58*, 380–388.

(14) (a) Aviram, A. ; Ratner, M. *Molecular Electronics: Science and Technology*; New York Academy of Sciences: New York, 1998. (b) Reed, M. A. ; Lee, T. *Molecular Nanoelectronics*; American Scientific Publishers: Los Angeles, CA, 2003.

(15) Selzer, Y.; Cai, L.; Cabassi, M. A.; Yao, Y.; Tour, J. M.; Mayer, T. S.; Allara, D. L. *Nano Lett.* **2005**, *5*, 61–65.

(16) Terrill, R. H.; Postlethwaite, T. A.; Chen, C.; Poon, C. D.; Terzis, A.; Chen, A.; Hutchison, J. E.; Clark, M. R.; Wignall, G.; Londono, J. D.; Superfine, R.; Falvo, M.; Johnson, C. S., Jr.; Samulski, E. T.; Murray, R. W. *J. Am. Chem. Soc.* **1995**, *117*, 12537–12548.

(17) Schmid, G.; Simon, U. *Chem. Commun.* **2005**, *697*, 710.

(18) Reed, M. A.; Zhou, C.; Muller, C. J.; Burgin, T. P.; Tour, J. M. *Science* **1997**, *278*, 252–254.

(19) (a) Chen, J.; Calvet, L. C.; Reed, M. A.; Carr, D. W.; Grubisha, D. S.; Bennett, D. W. *Chem. Phys. Lett.* **1999**, *313*, 741–748. (b) Tran, T. B.; Beloborodov, I. S.; Lin, X. M.; Bigioni, T. P.; Vinokur, V. M.; Jaeger, H. M. *Phys. Rev. Lett.* **2005**, *95*, Art. No. 076806.

(20) Frisch, M. J. ; Trucks, G. W.; Schlegel, H. B.; Scuseria, G. E.; Robb, M. A.; Cheeseman, J. R.; Montgomery, J. A., Jr.; Vreven, T.; Kudin, K. N.; Burant, J. C.; Millam, J. M.; Iyengar, S. S.; Tomasi, J.; Barone, V.; Mennucci, B.; Cossi, M.; Scalmani, G.; Rega, N.; Petersson, G. A.; Nakatsuji, H.; Hada, M.; Ehara, M.; Toyota, K.; Fukuda, R.; Hasegawa, J.; Ishida, M.; Nakajima, T.; Honda, Y.; Kitao, O.; Nakai, H.; Klene, M.; Li, X.; Knox, J. E.; Hratchian, H. P.; Cross, J. B.; Adamo, C.; Jaramillo, J.; Gomperts, R.; Stratmann, R. E.; Yazyev, O.; Austin, A. J.; Cammi, R.; Pomelli, C.; Ochterski, J. W.; Ayala, P. Y.; Morokuma, K.; Voth, G. A.; Salvador, P.; Dannenberg, J. J.; Zakrzewski, V. G.; Dapprich, S.; Daniels, A. D.; Strain, M. C.; Farkas, O.; Malick, D. K.; Rabuck, D.; Raghavachari, K.; Foresman, J. B.; Ortiz, J. V.; Cui, Q.; Baboul, A. G.; Clifford, S.; Cioslowski, J.; Stefanov, B. B.; Liu, G.; Liashenko, A.; Piskorz, P.;

Komaromi, I.; Martin, R. L.; Fox, D. J.; Keith, T.; Al-Laham, M. A.; Peng, C. Y.; Nanayakkara, A.; Challacombe, M.; Gill, P. M. W.; Johnson, B.; Chen, W.; Wong, M. W.; Gonzalez, C.; Pople, J. A. *Gaussian 03*, Revision C.02; Gaussian, Inc.: Pittsburgh, PA, 2004.

(21) Huang, W.; Masuda, G.; Maeda, S.; Tanaka, H.; Hino, T.; Ogawa, T. *Inorg. Chem.* **2008**, *47*, 468–480.

(22) Nitzan, A.; Ratner, M. A. *Science* **2003**, *300*, 1384–1389.

(23) Daniel, M. C.; Astruc, D. *Chem. Rev.* **2004**, *104*, 293–346.

(24) (a) Jernigan, J. C.; Surridge, N. A.; Zvanut, M. E.; Silver, M.; Murray, R. W. *J. Phys. Chem.* **1989**, *93*, 4620–4621. (b) Chen, S. W.; Murray, R. W. *J. Phys. Chem. B* **1999**, *103*, 9996–10000. (c) Barazzouk, S.; Kamat, P. V.; Hotchandani, S. *J. Phys. Chem. B* **2005**, *109*, 716–723.

(25) Huynha, M. H. V.; Dattelbauma, D. M.; Meyer, T. J. *Coord. Chem. Rev.* **2005**, *249*, 457–483.

(26) Carroll, R. L.; Corman, C. B. *Angew. Chem., Int. Ed* **2002**, *41*, 4378–4440.

(27) Erickson, N. E.; Sutin, N. *Inorg. Chem.* **1966**, *5*, 1834–1835.

(28) Araki, K.; Mizuguchi, E.; Tanaka, H.; Ogawa, T. *J. Nanosci. Nanotechnol.* **2006**, *6*, 708–712.

(29) *Crystalclear*, Version 1.3; MSC, Molecular structure Coorporation & Rigaku Coorporation: 9009 New Trails Drive, The Woodlands, TX, and Rigaku, Toyko, Japan, 2001.

(30) *TEXSAN*, Version 1.11; MSC, Molecular structure Coorporation & Rigaku Coorporation: 9009 New Trails Drive: The Woodlands, TX, and Rigaku, Toyko, Japan, 2000.

(31) Sheldrick, G. M. *SHELXTL*, Version 6.10, Software Reference Manual; Bruker AXS, Inc.: Madison, WI, 2000.

JP711635P